

# Evolution of the Stellar Mass Tully-Fisher Relation in Disk Galaxy Merger Simulations

Matthew D. Covington<sup>1</sup>

*Physics Department, University of California, Santa Cruz, CA 95064*

`covin039@umn.edu`

Susan A. Kassin

*Sub-Department of Astrophysics, University of Oxford, Oxford OX1 3RH, UK*

`s.kassin1@physics.ox.ac.uk`

Aaron A. Dutton

*UCO/Lick Observatory and Department of Astronomy, University of California, Santa Cruz, CA 95064*

Benjamin J. Weiner

*Steward Observatory, University of Arizona, Tucson, AZ 85721*

Thomas J. Cox

*Institute for Theory and Computation, Harvard-Smithsonian Center for Astrophysics, Cambridge, MA 02138*

Patrik Jonsson

*Santa Cruz Institute of Particle Physics, Santa Cruz, CA 95064*

Joel. R. Primack<sup>1</sup>

*Physics Department, University of California, Santa Cruz, CA 95064*

Sandra M. Faber

*UCO/Lick Observatory and Department of Astronomy, University of California, Santa Cruz, CA 95064*

David C. Koo

*UCO/Lick Observatory and Department of Astronomy, University of California, Santa Cruz, CA 95064*

---

<sup>1</sup>Santa Cruz Institute for Particle Physics, Santa Cruz, CA 95064

## ABSTRACT

There is a large observational scatter toward low velocities in the stellar mass Tully-Fisher relation if disturbed and compact objects are included. However, this scatter can be eliminated if one replaces rotation velocity with  $S_{0.5}$ , a quantity that includes a velocity dispersion term added in quadrature with the rotation velocity. In this work we use a large suite of hydrodynamic N-body galaxy merger simulations to explore a possible mechanism for creating the observed relations. Using mock observations of the simulations, we test for the presence of observational effects and explore the relationship between  $S_{0.5}$  and intrinsic properties of the galaxies. We find that galaxy mergers can explain the scatter in the TF as well as the tight  $S_{0.5}$ -stellar mass relation. Furthermore,  $S_{0.5}$  is correlated with the total central mass of a galaxy, including contributions due to dark matter.

*Subject headings:* galaxies: formation — galaxies: interactions — galaxies: kinematics and dynamics — galaxies: evolution

## 1. Introduction

One of the goals of a theory of galaxy formation is to reproduce the scaling relations of both early and late type galaxies. There has been significant work on understanding galaxy formation from analytic, semi-analytic, and numerical perspectives dating back to the collapsing gas cloud model of Eggen et al. (1962). For early type galaxies, scaling relations between their sizes, luminosities or stellar masses, and velocity dispersions form a two-dimensional plane called the “Fundamental Plane” (Dressler et al. 1987; Djorgovski & Davis 1987). For late type galaxies, a simple plane does not exist (Burstein et al. 1997), and the relation between luminosities or stellar masses and rotation velocities (i.e., the Tully-Fisher (TF) relation; Tully & Fisher 1977) is independent of size and surface brightness (e.g., Courteau & Rix 1999).

The Fundamental Plane was found to be a consequence of the virial theorem, if one assumes a constant mass-to-light ratio and homologous mass structure (Faber et al. 1987; Djorgovski & Davis 1987; Bender et al. 1993; Pahre et al. 1998). However, the situation is more complicated since there is a tilt observed between the Fundamental Plane and the plane resulting from the virial theorem. This tilt is likely due to a combination of stellar population effects and another factor which has yet to be determined (e.g., Pahre et al. 1998; Gerhard et al. 2001; Bertin et al. 2002; Hopkins et al. 2008). Hopkins et al. (2008) argue that this other factor results from a varying ratio of total enclosed mass within the effective radius ( $R_e$ ) to stellar mass. This ratio must depend on mass such that lower mass ellipticals are more baryon-dominated within  $R_e$  than their higher mass counterparts.

For disk galaxies, the scaling relations between velocity, luminosity or stellar mass, and size can broadly be understood by semi-analytic galaxy formation models which are based upon the dissi-

tionless collapse of a cold dark matter halo and angular momentum conservation (e.g., Mo et al. 1998; van den Bosch 2001; Dalcanton et al. 1997; de Jong & Lacey 2000; Dutton et al. 2007). Such models have their roots in the analytic formulations of White & Frenk (1991) and Fall & Efstathiou (1980) which in turn have their roots in the works of Silk (1977) and Rees & Ostriker (1977). A detailed prediction of disk galaxy scaling relations, which necessitates simultaneous matching of the zero-points of the TF relation, galaxy sizes, and the luminosity/stellar mass functions has proven elusive (e.g., Benson et al. 2003; Dutton et al. 2007). Models can be constructed that reproduce these properties (Dutton & van den Bosch 2009), but they require efficient mass outflows (a.k.a. feedback), and the absence of dark halo adiabatic contraction (Blumenthal et al. 1986). On the purely numerical front, hydrodynamic + N-body codes have been able to form disk-like systems only under controlled conditions and for halos carefully selected based upon their merger histories (e.g., Governato et al. 2004, 2007; Robertson et al. 2004; Scannapieco et al. 2009). Furthermore, the formation of realistic bulge-less galaxies remains an unsolved problem for cosmological simulations (e.g., Mayer et al. 2008).

Cosmological hydrodynamical simulations have been able to form galaxies with disks that reproduce the slope of the TF relation (e.g. Navarro & Steinmetz 2000; Eke et al. 2001, Portinari et al. 2007, Governato et al. 2007; Piontek & Steinmetz 2009). However, as with analytic and semi-analytic models, reproducing the TF zero point, and observed disk sizes has been a challenge. If the rotation velocity is measured at a radius which encloses most of the baryons, then simulated galaxies can reproduce the zero point of the TF relation (e.g. Governato et al. 2007). However, if the rotation velocity is measured at a smaller radius (such as 2.2 K-band disk scale lengths), the same simulations of Governato et al. (2007) over-predict the rotation velocities (Dutton & Courteau 2008). This failure is due to the simulations having the wrong distribution of baryons and/or dark matter within the optical parts of galaxies.

In summary, although the scaling relations of early and late type galaxies can be explained in broad terms, detailed predictions have yet to fully mature. In addition, since early type galaxies are generally expected to form through mergers of late type systems, the scaling relations of early types should therefore descend from those of late types. There has been work with simulations of mergers of late types to try to understand this (e.g., Robertson et al. 2006; Covington et al. 2008; Hopkins et al. 2009). Dekel & Cox (2006), Hopkins et al. (2008), and Covington et al. (in prep) in particular argue that late type scaling relations may evolve into those of early types if the varying gas content of disk galaxies with mass and dissipation during mergers are taken into account in models. However, not all galaxies in today’s universe are the well-ordered disk or elliptical systems for which most theories make predictions. Many galaxies have disturbed or irregular morphologies and/or kinematics, and the fraction of these galaxies increases with redshift to at least  $z \sim 1$  (see e.g., van den Bergh et al. 1996; Kassin et al. 2007, for morphologies and kinematics, respectively). With this in mind, we examine the findings of Kassin et al. (2007) which attempt to include such irregular systems in a study of the Tully-Fisher scaling relation, and to link early and late types through their kinematics.

In particular, we focus on the scaling laws that relate galactic orbital speeds to stellar masses: the TF relation (Tully & Fisher 1977) for rotating disk galaxies, which relates stellar mass to rotation velocity ( $V_{\text{rot}}$ ), and the Faber-Jackson relation (FJ) (Faber & Jackson 1976) for spheroidal (elliptical) galaxies, which relates stellar mass to velocity dispersion ( $\sigma$ ). The conventionally assumed pathway for forming ellipticals is through mergers of disk galaxies (Barnes & Hernquist 1992), in which case the FJ relation descended from the TF relation, as modified by mergers.

The TF and FJ relations relate the specific kinetic energy required to support a galaxy to the attractive potential well created by the mass of the galaxy. Using the DEIMOS multi-object spectrograph at Keck Observatory, Kassin et al. (2007) observed the kinematics and masses of emission line galaxies in a redshift range from 0.1 to 1.2 from the All Wavelength Extended Groth Strip International Survey (AEGIS), incorporating morphologically normal and disturbed galaxies. They find that the disturbed galaxies do not lie on the standard TF relation which only considers global rotational support. Many of the disturbed galaxies have rotation velocities that are well below the normal values. This morphological dependence of the TF scatter is well known. Studies of local galaxies have found larger scatter for close pairs of galaxies with kinematic disorders (Barton et al. 2001) and when peculiar galaxies are added (Kannappan et al. 2002). At  $z \sim 0.5$ , Flores et al. (2006) find larger TF scatter for galaxies with “complex kinematics,” which was confirmed by the larger sample and more detailed analysis of Puech et al. (2008). This correlation of scatter with morphology is not surprising, as one might expect kinematic scaling relations based on pure rotational support to fail for cases where the systems are not in globally ordered motion. Galaxies that are merging, disturbed, or rapidly evolving may exhibit disordered kinematics, so that considering only rotation will not capture all the kinematic support that balances the gravitational attraction of the potential.

Interestingly, when Weiner et al. (2006) and Kassin et al. (2007) incorporated the random internal motions of galaxies, as measured by velocity dispersion, along with rotational velocity into a new parameter,  $S_{0.5} = \sqrt{0.5V_{\text{rot}}^2 + \sigma^2}$ , then all galaxies regardless of morphology fell onto a single relation between  $S_{0.5}$  and stellar mass. This new parameter allowed for all galaxies to be incorporated in a measurement of the TF relation, instead of requiring the TF to be restricted to a sub-sample of galaxies selected to be morphologically and/or kinematically well-ordered. In addition, this new TF relation is consistent with the FJ relation for elliptical galaxies from Gallazzi et al. (2006). It is perhaps surprising that a set of non-homologous systems fall on the same kinematic relation, suggesting that the relation contains information on the kinematic evolution of galaxies.

Given the complexity of effects at work, the constraints that produce this tight kinematic relation are not clear. The velocity dispersion as measured in gas-phase kinematics by Weiner et al. (2006) and Kassin et al. (2007) appears to provide kinematic support similar to a thermalized velocity dispersion, but it probably represents spatially unresolved velocity gradients rather than truly randomized motions. Observational effects, such as blurring, can transform chaotic motions or spatially unresolved rotation into apparent dispersion. The  $S_{0.5}$  quantity is formulated to measure a total specific kinetic energy; although these systems are non-equilibrium, it is likely that the

virial theorem remains a good approximation for the balance between kinematics and gravitational potential. In order to investigate these possibilities and to explore the origin of the  $S_{0.5}$ -stellar mass relation, we analyze a large suite of hydrodynamical galaxy merger simulations. Mock observations of this simulation set provide kinematic data on isolated disk galaxies, disturbed galaxies, merging/overlapping galaxies, and elliptical merger remnants. The simulations allow for a comparison with observational results as well as a parallel analysis of intrinsic kinematics and observational effects.

## 2. Methods

### 2.1. Galaxy Merger Simulations

We exploit a large suite of binary galaxy merger simulations originally used to study feedback and star-formation in galaxy mergers. It provides a rich source of kinematic data for galaxies with a wide range of morphologies. For this study we use a selection of 50 merger simulations from this suite. For full details on the merger simulations we refer the reader to previous studies (Cox et al. 2004; Cox 2004; Cox et al. 2006, 2008), but we include a brief description here for completeness.

The numerical simulations performed in this work use the N-Body/SPH code GADGET (Springel et al. 2001). Hydrodynamics are included via the Lagrangian technique of smoothed particle hydrodynamics (SPH). We use the “conservative entropy” version of SPH (Springel & Hernquist 2002). Gas is assumed, for simplicity, to be a primordial plasma that can radiatively cool via atomic and free-free emission.

All of the numerical simulations presented here include star formation. Stars are formed in regions of gas that are above a critical density for star formation at a rate proportional to the local gas density and inversely proportional to the local dynamical time-scale. The efficiency of star formation is fixed by requiring star formation to follow the observed correlation between gas surface densities and star-formation rate (Kennicutt 1998).

We also include a simple prescription to simulate the effects of feedback from massive stars. This feedback acts to pressurize the interstellar medium and regulates the conversion of gas to stars. Details of this model and the parameter choices can be found in Cox et al. (2006). Specifically, the simulations studied in this paper used the *n2med* parameter set. Under these assumptions the gas pressure increases as the density squared; i.e, star-forming gas has a “stiff” equation of state.

The simulations adopt a gravitational softening length of  $h = 400$  pc for the dark matter particles and 100 pc for the stellar and gas particles. We remind the reader that, in GADGET, forces between neighboring particles become non-Newtonian for separations  $< 2.3$  times the gravitational softening length.

The disk galaxy models and orbits are cosmologically motivated, but the simulations are not

cosmological since the two galaxies are isolated. All mergers are binary mergers of disk galaxies. Rather than being produced by previous mergers, the progenitor disk galaxies are constructed in equilibrium and contain dark matter, an exponential stellar disk, an extended exponential gas disk, and some contain a dense central bulge. The dark matter halos are assumed to have an NFW profile, whereas the stellar bulges have a three-dimensional exponential profile. Bulge to disk stellar mass ratios vary from 0.02 to 0.25. The portion of the suite used in this study contains two types of progenitor galaxy models:

1. “Sbc” galaxies, which are modeled after local Sbc-type spirals, with a small bulge and an initial gas mass roughly equal to the initial stellar mass.
2. “G” galaxies, which span a range of mass, bulge fraction, and gas fraction. Their properties are taken from statistical samples of local late type galaxies, including the Sloan Digital Sky Survey (York et al. 2000).

The Sbc mergers are all major mergers of identical progenitors with a stellar disk of  $3.92 \times 10^{10} M_{\odot}$ , a gas disk of  $5.36 \times 10^{10} M_{\odot}$ , a stellar bulge of  $1.00 \times 10^{10} M_{\odot}$ , and a dark matter halo of  $81.2 \times 10^{10} M_{\odot}$ . The Sbc series contains the widest variation of initial merger orbits and orientations, with 17 different orbits run. This includes orbits with a wide range of pericentric distances, eccentricities between 0.6 and 1.0, and a variety of progenitor orientations, including prograde-prograde, prograde-retrograde, retrograde-retrograde, and some cases inbetween. The G series mergers include both major mergers between identical galaxies and mergers of galaxies with mass ratios between 1:1 and 1:50. For more detail on these models see Cox (2004), Cox et al. (2008), and Covington et al. (2008).

## 2.2. Mock Observations of the Simulations

In order to make comparisons with the observational results, we must first mock ‘observe’ the galaxies in the same manner as Kassin et al. (2007). They used an algorithm called ROTCURVE (Weiner et al. 2006). This algorithm was designed to obtain kinematic measurements for as many galaxies as possible by allowing model seeing-compensated rotation curves to be fit using only the 2-d spectra. ROTCURVE creates an intrinsic model for the emission intensity, velocity, and dispersion, blurs this model to simulate seeing, and fits the model to the data. The intrinsic model used is:

$$I(x, v) = G(x) \exp\left(-\frac{(v - V(x))^2}{2\sigma_{2d}^2}\right), \quad (1)$$

$$G(x) = \frac{I_{\text{tot}}}{\sqrt{2\pi}r_i} \exp\left(-\frac{(x - x_0)^2}{2r_i^2}\right), \quad (2)$$

$$V(x) = V_{\text{rot}} \frac{2}{\pi} \arctan(x/r_v), \quad (3)$$

where  $G(x)$  is an assumed Gaussian light distribution along the slit,  $V(x)$  is the rotation curve, with asymptotic velocity  $V_{\text{rot}}$  and knee radius  $r_v$ , and  $\sigma_{2d}$  is the velocity dispersion, which is assumed to be constant along the slit. In order to fit the spectra,  $I(x, v)$  is blurred using a 1-d Gaussian in the spatial direction. After blurring, moments are taken of the blurred model in the velocity direction in order to get values of average velocity and dispersion for each bin within the slit. These values are then compared against the observed rotation curve by computing a  $\chi^2$  value.  $\chi^2$  is then minimized via adjustments of  $V_{\text{rot}}$  and  $\sigma_{2d}$ . The other potentially adjustable parameter,  $r_v$ , is held fixed at 0.2 arcsecs. Observational results do not change significantly if  $r_v$  is varied within a reasonable range of 0.1 to 0.3 arcsec.

In order to analyze the simulations, we use an analogous algorithm. Each simulation has snapshots every 40-100 Myr, and each of these snapshots is viewed from 11 different evenly distributed angles. The simulations are assumed to be at three different redshifts ( $z \sim 0.03$ ,  $z \sim 0.3$ , and  $z \sim 1.0$ ), which approximately cover the redshift range in Kassin et al. We include the lowest redshift bin to examine the relation with very little blurring. This results in a sample of roughly 150,000 mock observations. Physical distances are converted to arcsecs given the assumed redshift of the observation, using cosmological parameters  $h = 0.7$ ,  $\Omega_m = 0.3$ , and  $\Omega_\Lambda = 0.7$ . The effects of seeing are taken into account by smearing particle positions using a Gaussian with  $\sigma = 0.3$  arcsecs. If the projected separation of the two galaxies is less than 0.7, arcsecs then the two galaxies are treated as one object. This allows us to include merging and overlapping galaxies in the sample. We orient the mock slit by fitting an ellipse to the simulated stellar density profile. All mock observations use a slit width of 1.0 arcsec as in the observations. The mock slit length varies with redshift beginning with a length of 4.0 arcsecs at  $z \sim 1$  and scaling with physical galaxy size, as in the observations.

Within the slit, stellar particles - either all stars or just new stars (see Section 4.2) - are separated into 0.1 arcsec bins, mimicking the pixel width in the observations. Rotation curves are calculated using the average velocities and dispersions of the particles in each bin. We fit  $G(x)$  to the bin stellar masses and calculate  $I(x, v)$  and  $V(x)$  as above. Unlike Weiner et al. (2006) and Kassin et al. (2007), we do not hold  $r_v$  fixed, but instead assume a value of 0.2 arcsecs at  $z \sim 1$  and scale that value with the physical size of the galaxy. If we do not scale  $r_v$  and the slit length with redshift, we get spurious systematic offsets in  $V_{\text{rot}}$  when comparing the lowest redshift bin with the two higher redshift bins. Inclination is also calculated, using the thin disk approximation as in the observational work, and is used to correct  $V_{\text{rot}}$  to edge-on. We remove all galaxies from the sample with inclinations less than 50 degrees, as we find that the inclination fits become unreliable below that value. Similarly, Kassin et al. remove the galaxies with inclinations less than 30 degrees. The observational sample is also cut for nearly edge-on disks (inclination greater than 70 degrees) because of dust effects on stellar mass estimates. Since the simulations do not suffer from this same limitation, we do not cut at large inclinations.

### 3. Comparison of the Simulations with Observations

#### 3.1. Evolution of a Single Galaxy Merger

To illustrate how the kinematics of galaxies change during a merger event, we follow the time evolution of a single galaxy merger. Even though this is only a specific example case from the set of simulations studied, it is typical of the mock observations of the other simulations, as evidenced by the results of Section 3.2. The simulation used for this study is a merger of two identical Sbc galaxies. Initially, the galaxies are set on a parabolic prograde-prograde orbit with a pericentric distance of 11.0 kpc. We depict the evolution of kinematic quantities during the merger viewed from a single angle (Figure 1), and follow the galaxies’ evolution on the kinematic relations (Figure 2, numbers). The merger is assumed to be at a redshift of one.

We start off at time=0 Gyr with the progenitors, which are designed to lie on the observed TF ridge-line. The progenitor is demarcated as ‘1’ in Figures 1 and 2. We follow one of the galaxies until the projected distance between the galaxies becomes less than 0.7 arcsecs after which we follow the merger as a single system. The merging galaxies have two encounters and merge during the second encounter. The first encounter occurs at 0.6 Gyr after the start of the simulation. This encounter results in a significant increase in the velocity dispersion by  $\sim 60 \text{ km s}^{-1}$  and a sharp decrease in the rotation velocity by  $\sim 55 \text{ km s}^{-1}$ . During this encounter, the galaxy appears morphologically disturbed, especially in its outer disk. Shortly following the encounter, at 0.7 Gyr, the galaxy is a slightly low rotation velocity outlier in the TF (‘2’ in Figures 1 and 2). Between the first and second/final encounters, the rotation velocity of the galaxy gradually increases by  $\sim 20 \text{ km s}^{-1}$  as tidal debris that was removed from the disk settles back. The final coalescence occurs at 1.75 Gyr after the start of the simulation (‘3’ in Figures 1 and 2). At coalescence, the galaxy’s rotation velocity drops abruptly to a meager  $20 \text{ km s}^{-1}$ . The mock observational slit now contains both the first progenitor and the remains of the second progenitor, which has been severely disrupted. Projection results in the overlapping of the two progenitors within the slit and pollutes the rotation curve, causing the dramatic decrease in rotational velocity. Consequently, the system lies furthest from the TF law at this time (‘3’ in Figures 1 and 2). At the final coalescence, we find an increase in the velocity dispersion by  $\sim 100 \text{ km s}^{-1}$ . From this point on, the kinematics are dominated by dispersion rather than rotation. The final stage (‘4’ in Figures 1 and 2) depicts the merger remnant, which is a rotating elliptical galaxy. In contrast to the other kinematic quantities,  $S_{0.5}$  remains relatively stable throughout the merger process, increasing primarily when the two progenitors combine to create a more massive system.

The tendency for rotation velocity to decrease as velocity dispersion increases during galaxy interactions and mergers provides a simple mechanism to explain the observed  $S_{0.5}$ -stellar mass relation and large scatter in the conventional TF. We note, however, that observed  $S_{0.5}$  is not strictly conserved, even when mass is constant. During a close encounter all of the ‘lost’ rotation is not immediately converted into velocity dispersion. Rather, the tendency during such an encounter is for the apparent rotation velocity to briefly drop to very low values while the velocity dispersion

increases only modestly. The effects of this lack of strict conservation of  $S_{0.5}$  fall within the scatter of the  $S_{0.5}$ -stellar mass relation.

### 3.2. Kinematic Relations for an Ensemble of Simulated Galaxy Mergers

In order to further test this explanation for the observed kinematic relations, we plot rotation velocity and  $S_{0.5}$  versus stellar mass for 500 randomly chosen snapshots from set of 50 merger simulations and compare to similar plots for 544 galaxies from Kassin et al. (2007) (Figure 2). Each of these snapshots is viewed from an angle chosen at random from the 11 different evenly distributed viewing angles. These 500 snapshots are analyzed assuming  $z \sim 0.03$ ,  $z \sim 0.3$ , and  $z \sim 1.0$ . We find that at all redshifts the simulated TF has a significant scatter to low  $V_{\text{rot}}$  (spanning  $\sim 1.5$  dex), similar to the observations. Furthermore, this scatter is correlated with close encounters. Sixty-four percent of the cases with scatter greater than 0.5 dex are encounters/mergers, whereas encounters/mergers are only 30% of the entire sample. The primary difference between the simulated and observed results is in the correlation between scatter and redshift. For the observations, scatter in the TF significantly increases at high redshift, whereas for the simulations, the scatter in the TF does not correlate strongly with redshift. This suggests that the observed evolution in scatter of the TF represents a real change in kinematics with redshift as opposed to an observational blurring effect.

If we incorporate random internal motions using  $S_{0.5}$ , then we find a single, relatively tight relation with stellar mass. Comparing different redshift bins we see that the slope fitted to the simulated galaxies stays within a range of  $\sim 2.8 - 2.9$ , whereas the observed slopes are typically slightly steeper but range between  $\sim 2.4 - 3.3$ . There is no significant trend in slope with redshift in either the observations or simulations. In the two higher redshift bins the scatter in  $S_{0.5}$  for the simulations is 0.08-0.09 dex. The intrinsic scatter in the observed relation ranges between 0.08 and 0.12 dex and also has no systematic trend with redshift. The lowest redshift bin for the simulated results does show more scatter (0.16 dex), but this is likely due to difficulty in fitting unblurred rotation curves of disturbed objects, which often do not look like the idealized arctan rotation curve. This is also outside of the range of the observations discussed in Kassin et al. (2007).

While a detailed quantitative comparison of the samples is not warranted because the galaxies in the simulation suite are not a statistically representative sample of the types of galaxies that one would expect to find in the real Universe, the agreement with the observed relations demonstrates that galaxy mergers and interactions are a mechanism that can create large scatter in the TF concurrent with low scatter in the  $S_{0.5}$ -stellar mass relation.

Furthermore, the simulated results show that the merging process moves galaxies up the  $S_{0.5}$ -stellar mass relation toward higher values of  $S_{0.5}$ , and therefore that the relation ties together progenitors (spirals), merging galaxies, and merger remnants (ellipticals). The robustness of this relation has two causes. First, throughout the merger process there is a tendency for rotation and

velocity dispersion (or, random internal motions) to be anti-correlated. It has been known for a long time that galaxy mergers are an effective mechanism for converting ordered rotational support into random pressure support (Toomre & Toomre 1972). As noted above, it is surprising that a kinematic relation would hold for even merging cases. This results from a subtly different cause. Much of the apparent rotation velocity may be lost in an encounter when the two galaxies overlap in projection. This is because the two galaxies’ orbital velocities and internal velocities rarely add coherently when randomly overlapped. However, velocity dispersions are not so easily lost. In fact, overlapping two galaxies with interfering rotation curves will increase velocity dispersion. Thus, when such an overlap occurs, apparent rotation typically decreases, whereas velocity dispersion typically increases.

#### 4. Observational Effects on the $S_{0.5}$ -Stellar Mass Relation.

From the observations alone, it is unclear the extent to which the  $S_{0.5}$ -stellar mass relation is a result of observational effects or is telling us something about the intrinsic properties of the galaxies. In this section, we explore the various observational effects on the kinematic measurements of the simulations and determine whether they can contribute to the observed relation.

##### 4.1. Blurring

As galaxies are observed at higher redshifts, their angular extent becomes smaller. Consequently, the typical  $\sim 0.7''$  seeing produced by the atmosphere in the Kassin et al. observations effectively moves the stars from one spectral bin into other nearby bins within the slit. This reduces the apparent rotation velocity and produces an artificial velocity dispersion (Weiner et al. 2006). The fitting algorithm used by ROTCURVE takes this into account by fitting a blurred model and extrapolating back to an intrinsic model. However, an interesting question is how successful this procedure is, and whether or not blurring conserves  $S_{0.5}$ . If  $S_{0.5}$  is conserved by blurring, then it is possible that blurring is partially responsible for the scatter in the TF and the tight  $S_{0.5}$  relation.

In order to explore the effects of blurring, we take the fiducial merger simulation from §3.1 (the Sbc) and analyze the kinematics after blurring the particles using gaussians with  $\sigma$ ’s of  $0.0''$ ,  $0.1''$ ,  $0.3''$ ,  $0.6''$ ,  $0.8''$ , and  $1.6''$ , assuming the galaxy is at a redshift  $z \sim 1$  (Figure 3). We use the four example snapshots from Figure 1: the undisturbed disk, disturbed disk, merger, and merger remnant. The effective blurring within the AEGIS sample is all between  $0.1''$  and  $0.3''$ , given seeing of  $0.7''$  (defined as full-width at half maximum). There is little difference between the unblurred kinematics and  $0.1''$  kinematics for all snapshots shown. However, for both the disks and the remnant there is a decrease in  $V_{\text{rot}}$  and increase in  $\sigma$  by the time we have reached  $0.3''$ . However, for all cases, the decrease in  $V_{\text{rot}} \leq 30\%$ . Also, for all cases, as the blurring becomes much greater than  $R_{50}$ , the radius that contains 50% of the stellar mass, the ROTCURVE algorithm breaks down

and  $V_{\text{rot}}$  drops to very low values while  $\sigma$  rises.

For the undisturbed disk, disturbed disk, and merger,  $S_{0.5}$  is approximately conserved by blurring as  $V_{\text{rot}}$  and  $\sigma$  adjust in lockstep. However, for the remnant, by 0.3" blurring,  $S_{0.5}$  has already increased by  $\sim 50\%$ . This results from a steeply-peaked central velocity dispersion. For zero blurring, the assumption of a constant  $\sigma$  underestimates the kinetic energy contribution from random motion because the central peak is small with respect to the size of the slit. As this peak gets blurred, the fit improves.

Therefore, it is true that as blurring becomes very large ( $\gg R_{50}$ ), the ROTCURVE fitting procedure will break down and the rotational component of the kinematics will transform into dispersion. Also, for three of the four cases shown,  $S_{0.5}$  is conserved throughout this process. Therefore it is true that blurring could cause some additional spread in the TF and that using  $S_{0.5}$  rather than rotation velocity would help to reduce this spread. However, for the range of blurring and galaxy sizes in the observational study, the ROTCURVE model performs relatively well, and certainly does not produce large enough errors to low  $V_{\text{rot}}$  to account for the observed scatter. This is also confirmed by the apparent lack of systematic changes in  $V_{\text{rot}}$  with redshift in Figure 2. Thus blurring cannot be the main reason for the observational findings.

## 4.2. Tracking of Emission Lines

A potential concern with our analysis is that the AEGIS observational results rely on OII 3727 emission line spectra from hot gas, whereas the kinematic analysis of the simulations described above uses the star particles. Specifically, the line emission is known to be correlated with areas of new star formation. Thus, we repeat the analysis from §3.2 using only new stars that form in the simulation and assuming  $z = 1$  (Figure 4). This gives us many fewer particles to work with, especially in the early stages of the merger when few new stars have formed. In order to provide sufficient statistics within the slit, we restrict the analysis to snapshots that have greater than 500 new star particles. This removes some of the sample from early on in the simulations, but will provide a check for whether or not limiting the analysis to new stars affects the results.

The TF and  $S_{0.5}$  relations are qualitatively quite similar to those calculated using all star particles, showing large scatter for TF and relatively small scatter for  $S_{0.5}$ . This suggests that the observational difference between tracing kinematics using hot gas and stars does not have a significant effect on the results. There is some additional scatter in the new star  $S_{0.5}$  relation (0.14 dex as compared to 0.08 dex). However, one must also remember that dust, which is not taken into account in the simulations, creates a counteracting effect. Within the simulations, analyzing only new stars will emphasize the central portions of the galaxies (where most stars form), however, these also tend to be the portions of the galaxy most enshrouded by dust. Thus, the real difference between observing emission lines (gas) or absorption lines (stars) is likely to be less. In order to truly pin down the effect of dust, one would have to create artificial spectral kinematics by fully

modeling the radiative transfer through the gas and dust. This will soon be possible using a newer version of SUNRISE (Jonsson, 2006 and in preparation).

## 5. Intrinsic Kinematic Quantities

We have explored some of the observational effects on the kinematic relations, however, we can further utilize the simulations to examine intrinsic kinematic quantities in order to better understand the origin of the  $S_{0.5}$ -stellar mass relation. If one assumes a tracer population within an isothermal sphere at a distance  $r \gg r_{\text{core}}$ , where  $r_{\text{core}}$  is the core radius of the isothermal sphere, and then allows that population to assume complete rotational support or complete support from random motion then one finds that  $V_{\text{circ}} \sim \sqrt{2}\sigma$ , where  $V_{\text{circ}}$  is the velocity with pure circular support and  $\sigma$  is the dispersion for pure random support (Weiner et al. 2006; Kassin et al. 2007). This was the motivation for the multiplying factor of 1/2 in front of  $V_{\text{rot}}$  in  $S_{0.5}$ . One might expect that a smooth transition between rotational and random support, while conserving the density profile, would result in conservation of  $S_{0.5}$ . Therefore, an important question is whether this idealized picture is correct and  $S_{0.5}$  really does trace the mass distribution. If so, this would provide a means of estimating total masses of galaxies including the contribution from dark matter.

### 5.1. Kinematics as a Function of Radius

We begin our analysis of intrinsic galaxy properties by examining kinematics as a function of radius. The  $S_{0.5}$  parameter is motivated by results obtained from the Jeans Equations for an isothermal sphere. However, our systems are not isothermal spheres, so we take a step back to see where the assumptions could be wrong. For steady state spherically symmetric systems with no rotation, the following relation holds (Binney and Tremaine, 1987, eq. (4-55)):

$$V_{\text{circ}}^2 = \frac{GM(r)}{r} = -\overline{\sigma_r^2} \left( \frac{d \ln \nu}{d \ln r} + \frac{d \ln \overline{\sigma_r^2}}{d \ln r} + 2\beta \right), \quad (4)$$

where  $\sigma_r$  is the radial velocity dispersion,  $\nu$  is the mass density,  $\beta \equiv 1 - \sigma_\theta^2/\sigma_\phi^2$  is the velocity anisotropy parameter, and  $\sigma_\theta$  and  $\sigma_\phi$  are the velocity dispersions in the  $\theta$  and  $\phi$  directions. At a given radius, this can be represented as the simpler

$$V_{\text{circ}}^2 = k\sigma_r^2. \quad (5)$$

For the singular isothermal sphere, the second two terms in the parentheses are zero and we are left only with  $V_{\text{circ}}^2 = -\overline{\sigma_r^2}(d \ln \nu/d \ln r)$ . For an isothermal sphere with a core radius  $r_{\text{core}}$  and  $r \gg r_{\text{core}}$  the density term  $(d \ln \nu)/(d \ln r) \sim -2$ , giving us the constant,  $k \sim 2$ , in the  $S_{0.5}$  relation. For our simulation set, and for real galaxies, we are neither guaranteed that the density

term will be  $\sim -2$  nor that the other two terms will vanish. Thus we look in detail at the values these terms are likely to have.

The velocity dispersion is generally a weak function of radius. Thus the dispersion term,  $d(\ln \overline{\sigma_r^2})/d(\ln r)$  is likely to be relatively small. The drop in dispersion with radius is quite small in the progenitors and is largest for the remnants, where significant dissipation and star formation may have steepened the profiles. As shown in Dekel et al. (2005) the dispersion in the remnants is relatively well represented by  $\sigma \propto r^{-0.2}$ . Thus the contribution of the dispersion term in equation 4 is likely to be  $-0.2$  or smaller, which is quite small compared to the presumed value of the density term. Because of tidal disturbance and dissipation, the stellar orbits in the outer portions of the merger remnants do exhibit relatively large anisotropies with  $\beta \sim 0.2 - 0.5$  (Dekel et al. 2005). Furthermore this term is multiplied by a factor of two bringing the overall contribution to  $\sim 0.4 - 1.0$ . For progenitors, which typically have low anisotropies, one would expect the contributions from these terms to roughly cancel, whereas for remnants there would be a net contribution to  $k$  of  $\sim 0.2 - 0.8$ .

The largest of the three terms is the density term. This term has a value of roughly two for an isothermal sphere and three or four for the outer portion of an NFW or a Hernquist profile. Thus we very well might expect a steeper density relation,  $\rho \propto r^{-a}$ , and consequently higher value of  $k$  than is found for the isothermal case. For each simulation we fit a value of  $a$  to the total mass density curve in the vicinity of  $R_{50}$ , the radius that contains 50% of the stellar mass. For the simulations, the value of  $a$  at  $R_{50}$  ranges between  $\sim 1.5 - 3.5$ , with a peak around negative two (see Figure 5). The slope is typically steeper for massive progenitors and for merger remnants. In summary, for progenitors, the density term is likely to be  $\sim 2$ , while the other terms will be small. For remnants, the density term will often be closer to 3, but the anisotropy term is likely to counteract much of this effect. So for all cases,  $k \sim 2$  is a reasonable value, but the variability in the density profiles and kinematics is sure to produce variation around this value.

For our exploration of intrinsic galaxy quantities, we adopt a quantity,  $S \equiv \sqrt{V_{\text{rot}}^2 + 2.0\sigma^2}$ , which is just  $\sqrt{2}S_{0.5}$  but with the benefit that it approaches  $V_{\text{rot}}$  in the low- $\sigma$  limit. This provides a quantity that can be directly compared with the velocity due to all mass,  $V_{\text{circ}}$ . The constant  $k$  is a function of radius, and therefore it is useful to determine the range in radius for which  $k \sim 2$ , or alternatively  $S \sim V_{\text{circ}}$ . In order to examine the value of  $k$  as a function of radius, we stack all of the simulated galaxies, normalizing radii to  $R_{50}$ . For this analysis, we separate the particles into bins of width equal to  $0.2R_{50}$ . For each bin, we determine an average velocity and velocity dispersion for the stellar particles. This provides us with intrinsic quantities analogous to  $V_{\text{rot}}$  and  $\sigma$ . These values are used to calculate  $S_{\text{intrinsic}}$ .  $V_{\text{circ}} \equiv \sqrt{GM(< r)/r}$  is calculated for each bin by totaling the masses of all particles with a radius less than the bin, including baryons and dark matter. In Figure 6, we plot the ratio of  $S_{\text{intrinsic}}$  and  $V_{\text{circ}}$  as a function of radius averaged over the velocity profiles of every snapshot within the simulation suite. One can see that at small radii there is no one-to-one correspondence between  $S_{\text{intrinsic}}$  and  $V_{\text{circ}}$  as the ratio ( $S_{\text{intrinsic}}/V_{\text{circ}}$ ) becomes closer to 2 or 3 on average with a large scatter between simulated profiles. However, at radii equal to or larger than

$R_{50}$ , the ratio is quite close to unity and the scatter is about 30% in either direction. Therefore, at radii larger than  $R_{50}$ ,  $S_{\text{intrinsic}}$  is a good indicator of total enclosed mass. For simplicity, we choose a radius of  $R_{50}$  at which to draw a value of  $S_{\text{intrinsic}}$  for comparison across the entire sample.

### 5.2. Correlation between $S_{\text{intrinsic}}$ and $V_{\text{circ}}$

Now that we have demonstrated that  $S_{\text{intrinsic}}$  is roughly comparable to  $V_{\text{circ}}$  at  $R_{50}$ , it is illustrative to plot the relation between  $S_{\text{intrinsic}}$  and  $V_{\text{circ}}$  for the sample. We take these values at  $R_{50}$  and plot them for 500 randomly chosen snapshots in Figure 7. If the two galaxies were separated by less than the sum of their stellar half-mass radii then they were treated as one. The  $x = y$  line represents equality between the two values. One can see that  $S_{\text{intrinsic}}$  is a good indicator of enclosed mass. The scatter in the relation increases with mass. This is the result of the distribution of galaxy types in the simulations. There are considerably more simulations run for the larger galaxies, and these simulations have a wide variety of orbits that can introduce significant spread in remnant properties (Covington et al. 2008). Therefore our simulation set will automatically produce more spread at higher masses. However, even for the larger mass cases, whose spread is likely more representative of the real universe than the low mass cases,  $\log(S_{\text{intrinsic}}) \sim \log(V_{\text{circ}})$  to typically within 0.15 dex.

### 5.3. Correlation between $S_{\text{observed}}$ and Intrinsic $V_{\text{circ}}$

A final question of interest is whether or not the observed quantity,  $S$ , can be used to estimate total galaxy mass, including the contribution from dark matter. To address this question, we plot the relation between  $S_{\text{observed}}$  and the *intrinsic*  $V_{\text{circ}}$  in Figure 8. Again, we have moved the factor of 2 in the  $S_{0.5}$  quantity over to the  $\sigma$  in order to produce a correspondence between  $S_{\text{observed}}$  and  $V_{\text{circ}}$ . Here we calculated a projected  $R_{50}$  using an elliptical aperture and measure a three-dimensional  $V_{\text{circ}}$  within that radius. The  $V_{\text{rot}}$  values are taken as the value of the fitted arctan curve at  $R_{50}$  rather than the asymptotic value. The observations are assumed to be at a redshift of one. As can be seen in Figure 8, there is a rough correspondence between  $S_{\text{observed}}$  and  $V_{\text{circ}}$ . Therefore, we take this result as a confirmation that  $S_{\text{observed}}$  can be used to track central galaxy mass, including contributions from dark matter. There is a tendency for  $S_{\text{observed}}$  to be a bit lower than  $V_{\text{circ}}$ . This is likely the result of projection effects and counter-rotation, both of which would serve to reduce  $S_{\text{observed}}$  compared with  $S_{\text{intrinsic}}$ . The outliers to low  $S_{\text{observed}}$  are typically overlapping cases where the kinematics are poorly represented by an arctan curve. The fact that the intrinsic relation is significantly better than the observed one suggests that it may be possible to improve the observational measurement of  $S$ . The assumptions of the arctan rotation curve and flat velocity dispersion often fail for the simulated galaxies, particularly when two galaxies overlap. Future work should examine possible improvements to the observational algorithm.

## 6. Discussion

The observational results from Kassin et al. (2007) were interesting for several reasons. They demonstrated that a new kinematic quantity,  $S_{0.5}$ , was capable of producing a relation that unified all galaxy types, including disturbed and merging cases. However, this study left open several questions that cannot be answered from the observations alone. First, what sort of mechanisms could produce the large scatter in the stellar mass TF while preserving the  $S_{0.5}$ -stellar mass relation? A second question is whether the relation is telling us something deep about the observed galaxies, or whether it is an artifact from the observations. Here we used a suite of galaxy merger simulations to address these questions.

We find that galaxy mergers and interactions are capable of reproducing the observed relation. Specifically, there are merger stages during which the galaxies overlap and the rotation velocity significantly drops. This overlap results in increased dispersion which when included in a kinematic relation helps to reduce the scatter. Additionally, within a given merger one can see that rotational support is transformed into random pressure support. This transformation occurs in such a way that the scaling between  $\log(S_{0.5})$  and  $\log(M_{\text{star}})$  is roughly conserved. Thus, galaxy mergers move galaxies up along the  $S_{0.5}$ -stellar mass relation, and the relation effectively unifies progenitors, mergers, and remnants.

We examine the observational effect of blurring to see whether it could be responsible for the observed additional dispersion and lack of rotation. We find that the ROTCURVE algorithm performs well for the range of blurring found in the observations. We also find that  $S_{0.5}$  is typically conserved by blurring. Therefore it could be responsible for some of the reduction in scatter, but the effect is much too small to account for the small observed scatter in the  $S_{0.5}$ -stellar mass relation.

Our examination of the kinematic scaling laws of the galaxies, and how they change with radius suggests that the appropriate constant in the  $S_{0.5}$  parameter is  $\sim 2$ . Additionally, we find that  $S$  at  $R_{50}$  is a reasonably good tracer of  $V_{\text{circ}}$  at  $R_{50}$ . Therefore, it can be used to infer the galaxy mass within  $R_{50}$ , including contributions from dark matter. However, the details of this relation warrant more study. Specifically, the relation between  $S_{\text{intrinsic}}$  and  $V_{\text{circ}}$  is much better than that with  $S_{\text{observed}}$ , suggesting that it may be possible to improve the observational measurement of  $S$  and consequently of the total enclosed mass. Additionally, it would be interesting to compare the merger simulations with available integral field unit observations of nearby,  $z \sim 0.6$ , and  $z \sim 2$  galaxies (e.g. Arribas et al. 2008; Yang et al. 2008; Förster Schreiber et al. 2006, respectively). It is also likely that kinematics could be used as an indicator for merging galaxies, and possibly merger stage, since mergers often produce TF outliers and typically have significant asymmetry in their kinematics, but the development of new kinematic indicators of merging is left for future work.

## 7. Acknowledgments

MDC acknowledges support from NASA ATP grant NNX07AG94G, the UCSC Physics Department, and a UCSC UARC-ARP grant. JRP was supported by NASA ATP grant NNX07AG94G. Simulations analyzed here were carried out at NERSC, NASA’s Columbia supercomputer, and UCSC computer clusters.

## REFERENCES

- Arribas, S., Colina, L., Monreal-Ibero, A., Alfonso, J., García-Marín, M., & Alonso-Herrero, A. 2008, *A&A*, 479, 687
- Barnes, J. E. & Hernquist, L. 1992, *ARA&A*, 30, 705
- Barton, E. J., Geller, M. J., Bromley, B. C., van Zee, L., & Kenyon, S. J. 2001, *AJ*, 121, 625
- Bender, R., Burstein, D., & Faber, S. M. 1993, *ApJ*, 411, 153
- Benson, A. J., Bower, R. G., Frenk, C. S., Lacey, C. G., Baugh, C. M., & Cole, S. 2003, *ApJ*, 599, 38
- Bertin, G., Ciotti, L., & Del Principe, M. 2002, *A&A*, 386, 149
- Blumenthal, G. R., Faber, S. M., Flores, R., & Primack, J. R. 1986, *ApJ*, 301, 27
- Burstein, D., Bender, R., Faber, S., & Nolthenius, R. 1997, *AJ*, 114, 1365
- Conselice, C. J., Bundy, K., Ellis, R. S., Brichmann, J., Vogt, N. P., & Phillips, A. C. 2005, *ApJ*, 628, 160
- Courteau, S. & Rix, H.-W. 1999, *ApJ*, 513, 561
- Covington, M., Dekel, A., Cox, T. J., Jonsson, P., & Primack, J. R. 2008, *MNRAS*, 384, 94
- Covington, M., Croton, D., Somerville, R., Primack, J., Cox, T. J., Jonsson, P., & Dekel, A., in prep
- Cox, T. J. 2004, PhD thesis, UC Santa Cruz
- Cox, T. J., Jonsson, P., Primack, J. R., & Somerville, R. S. 2006, *MNRAS*, 373, 1013
- Cox, T. J., Jonsson, P., Somerville, R. S., Primack, J. R., & Dekel, A. 2008, *MNRAS*, 384, 386
- Cox, T. J., Primack, J., Jonsson, P., & Somerville, R. S. 2004, *ApJ*, 607, L87
- Dalcanton, J. J., Spergel, D. N., & Summers, F. J. 1997, *ApJ*, 482, 659

- de Jong, R. S. & Lacey, C. 2000, *ApJ*, 545, 781
- Dekel, A. & Cox, T. J. 2006, *MNRAS*, 370, 1445
- Dekel, A., Stoehr, F., Mamon, G. A., Cox, T. J., Novak, G. S., & Primack, J. R. 2005, *Nature*, 437, 707
- Djorgovski, S. & Davis, M. 1987, *ApJ*, 313, 59
- Dressler, A., Faber, S. M., Burstein, D., Davies, R. L., Lynden-Bell, D., Terlevich, R. J., & Wegner, G. 1987, *ApJ*, 313, L37
- Dutton, A. A. & van den Bosch, F. C. 2009, *MNRAS*, 396, 141
- Dutton, A. A., & Courteau, S. 2008, *Astronomical Society of the Pacific Conference Series*, 396, 463
- Dutton, A. A., van den Bosch, F. C., Dekel, A., & Courteau, S. 2007, *ApJ*, 654, 27
- Eggen, O. J., Lynden-Bell, D., & Sandage, A. R. 1962, *ApJ*, 136, 748
- Eke, V. R., Navarro, J. F., & Steinmetz, M. 2001, *ApJ*, 554, 114
- Faber, S. M., Dressler, A., Davies, R. L., Burstein, D., & Lynden-Bell, D. 1987, in *Nearly Normal Galaxies. From the Planck Time to the Present*, ed. S. M. Faber, 175–183
- Faber, S. M. & Jackson, R. E. 1976, *ApJ*, 204, 668
- Fall, S. M. & Efstathiou, G. 1980, *MNRAS*, 193, 189
- Flores, H., Hammer, F., Puech, M., Amram, P., & Balkowski, C. 2006, *A&A*, 455, 107
- Förster Schreiber, N. M., Genzel, R., Lehnert, M. D., Bouché, N., Verma, A., Erb, D. K., Shapley, A. E., Steidel, C. C., Davies, R., Lutz, D., Nesvadba, N., Tacconi, L. J., Eisenhauer, F., Abuter, R., Gilbert, A., Gillessen, S., & Sternberg, A. 2006, *ApJ*, 645, 1062
- Gallazzi, A., Charlot, S., Brinchmann, J., & White, S. D. M. 2006, *MNRAS*, 370, 1106
- Gerhard, O., Kronawitter, A., Saglia, R. P., & Bender, R. 2001, *AJ*, 121, 1936
- Governato, F., Mayer, L., Wadsley, J., Gardner, J. P., Willman, B., Hayashi, E., Quinn, T., Stadel, J., & Lake, G. 2004, *ApJ*, 607, 688
- Governato, F., Willman, B., Mayer, L., Brooks, A., Stinson, G., Valenzuela, O., Wadsley, J., & Quinn, T. 2007, *MNRAS*, 374, 1479
- Hopkins, P. F., Cox, T. J., & Hernquist, L. 2008, *ApJ*, 689, 17
- Hopkins, P. F., Hernquist, L., Cox, T. J., Keres, D., & Wuyts, S. 2009, *ApJ*, 691, 1424

- Jonsson, P., Cox, T. J., Primack, J. R., & Somerville, R. S. 2006, *ApJ*, 637, 255
- Kannappan, S. J., Fabricant, D. G., & Franx, M. 2002, *AJ*, 123, 2358
- Kassin, S. A., Weiner, B. J., Faber, S. M., Koo, D. C., Lotz, J. M., Diemand, J., Harker, J. J., Bundy, K., Metevier, A. J., Phillips, A. C., Cooper, M. C., Croton, D. J., Konidaris, N., Noeske, K. G., & Willmer, C. N. A. 2007, *ApJ*, 660, L35
- Kennicutt, R. C. 1998, *ApJ*, 498, 541
- Mayer, L., Governato, F., & Kaufmann, T. 2008, *Advanced Science Letters*, 1, 7
- Mo, H. J., Mao, S., & White, S. D. M. 1998, *MNRAS*, 295, 319
- Navarro, J. F., & Steinmetz, M. 2000, *ApJ*, 538, 477
- Pahre, M. A., Djorgovski, S. G., & de Carvalho, R. R. 1998, *AJ*, 116, 1591
- Piontek, F., & Steinmetz, M. 2009, arXiv:0909.4167
- Portinari, L., & Sommer-Larsen, J. 2007, *MNRAS*, 375, 913
- Puech, M., Flores, H., Hammer, F., Yang, Y., Neichel, B., Lehnert, M., Chemin, L., Nesvadba, N., Epinat, B., Amram, P., Balkowski, C., Cesarsky, C., Dannerbauer, H., di Serego Alighieri, S., Fuentes-Carrera, I., Guiderdoni, B., Kembhavi, A., Liang, Y. C., Östlin, G., Pozzetti, L., Ravikumar, C. D., Rawat, A., Vergani, D., Vernet, J., & Wozniak, H. 2008, *A&A*, 484, 173
- Rees, M. J. & Ostriker, J. P. 1977, *MNRAS*, 179, 541
- Robertson, B., Cox, T. J., Hernquist, L., Franx, M., Hopkins, P. F., Martini, P., & Springel, V. 2006, *ApJ*, 641, 21
- Robertson, B., Yoshida, N., Springel, V., & Hernquist, L. 2004, *ApJ*, 606, 32
- Scannapieco, C., White, S. D. M., Springel, V., & Tissera, P. B. 2009, *MNRAS*, 396, 696
- Silk, J. 1977, *ApJ*, 211, 638
- Springel, V. & Hernquist, L. 2002, *MNRAS*, 333, 649
- Springel, V., Yoshida, N., & White, S. D. M. 2001, *New Astronomy*, 6, 79
- Toomre, A. & Toomre, J. 1972, *ApJ*, 178, 623
- Tully, R. B. & Fisher, J. R. 1977, *A&A*, 54, 661
- van den Bergh, S., Abraham, R. G., Ellis, R. S., Tanvir, N. R., Santiago, B. X., & Glazebrook, K. G. 1996, *AJ*, 112, 359

van den Bosch, F. C. 2001, MNRAS, 327, 1334

Weiner, B. J., Willmer, C. N. A., Faber, S. M., Melbourne, J., Kassin, S. A., Phillips, A. C., Harker, J., Metevier, A. J., Vogt, N. P., & Koo, D. C. 2006, ApJ, 653, 1027

White, S. D. M. & Frenk, C. S. 1991, ApJ, 379, 52

Yang, Y., Flores, H., Hammer, F., Neichel, B., Puech, M., Nesvadba, N., Rawat, A., Cesarsky, C., Lehnert, M., Pozzetti, L., Fuentes-Carrera, I., Amram, P., Balkowski, C., Dannerbauer, H., di Serego Alighieri, S., Guiderdoni, B., Kembhavi, A., Liang, Y. C., Östlin, G., Ravikumar, C. D., Vergani, D., Vernet, J., & Wozniak, H. 2008, A&A, 477, 789

York, D. G., Adelman, J., Anderson, Jr., J. E., Anderson, S. F., Annis, J., Bahcall, N. A., Bakken, J. A., Barkhouser, R., Bastian, S., Berman, E., Boroski, W. N., Yanny, B., & Yasuda, N. 2000, AJ, 120, 1579

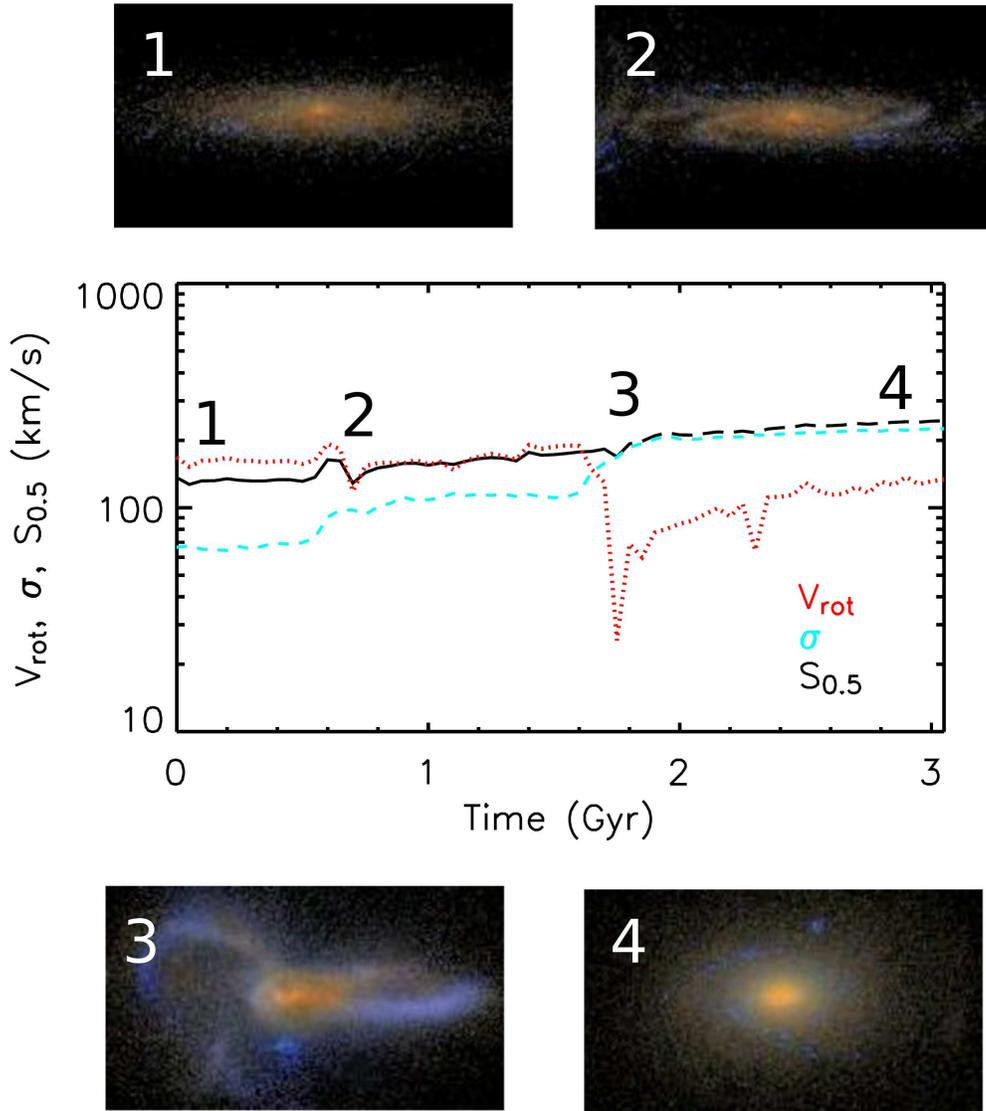


Fig. 1.—

Fig. 1.— Time evolution of rotation velocity (red dotted line), velocity dispersion (blue dashed line), and  $S_{0.5}$  (solid and long-dashed black lines) during a single merger simulation of two Sbc galaxies with stellar masses of  $\sim 5 \times 10^{10} M_{\odot}$  initially on a parabolic orbit. With each encounter, the rotation velocity decreases and the integrated velocity dispersion increases. However,  $S_{0.5}$  remains relatively constant throughout the merger, increasing primarily when the two galaxies coalesce. Care is taken to mock observe the simulations just as in the actual observations, assuming  $z = 1$ . The solid portion of the  $S_{0.5}$  line denotes the snapshots where only a single progenitor is observed in the slit, and the long-dashed portion denotes snapshots where both progenitors are observed in the slit. The merger simulation uses the smoothed-particle hydrodynamics code GADGET (Springel et al. 2001) and includes gas, star formation, and stellar feedback. The galaxy images are calculated from the simulation using the dust radiative transfer code SUNRISE (Jonsson et al. 2006) and are shown at four different times during the merger: 1) Before any encounters, 2) shortly after the initial encounter, 3) at the final coalescence, and 4) the remnant after the galaxies have coalesced.

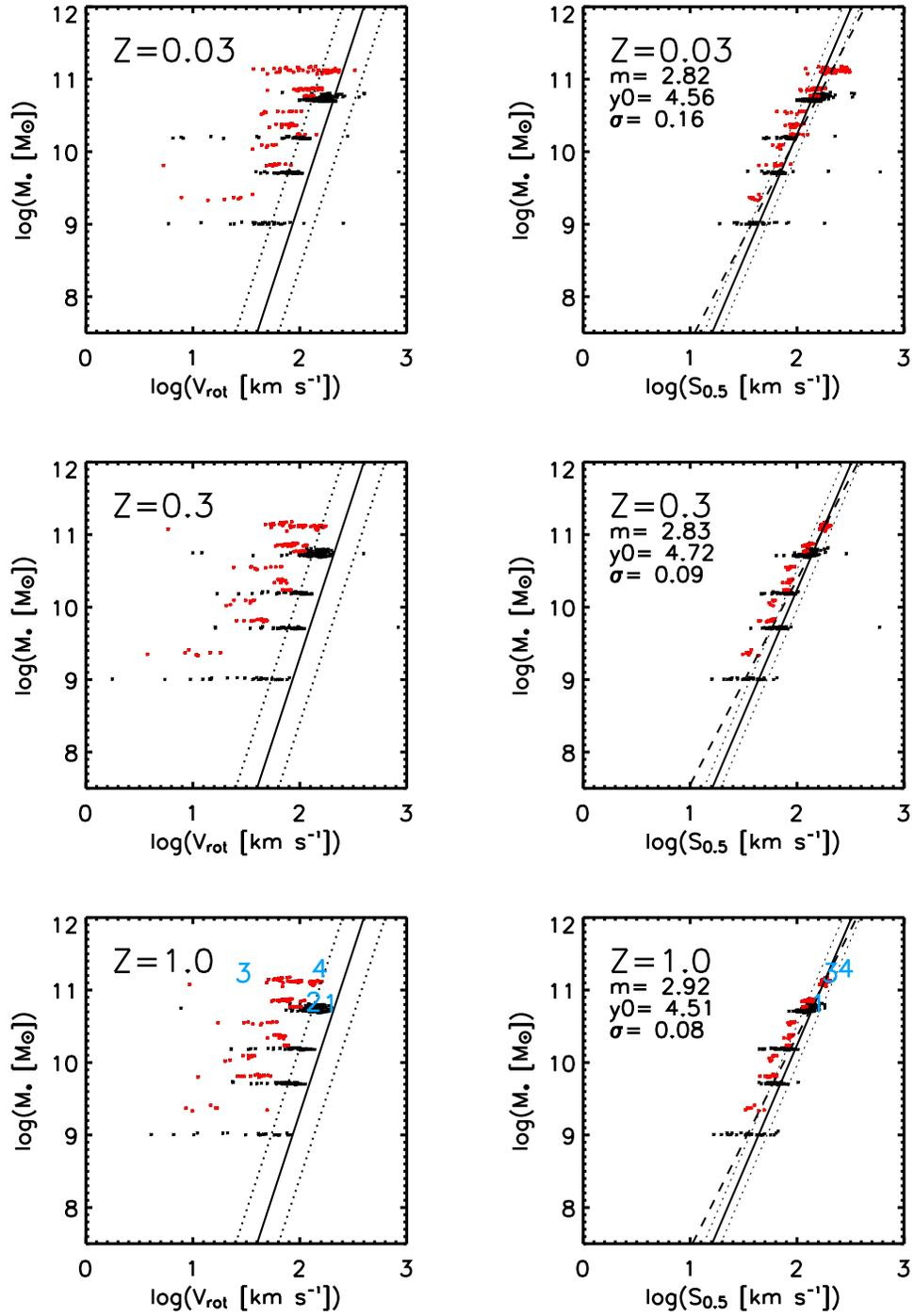


Fig. 2.—

Fig. 2.— The TF relation (left) and  $S_{0.5}$ -stellar mass relation (right) for mock observations of simulated merging galaxies at redshifts of  $z \sim 0.03$  (top),  $z \sim 0.3$  (middle), and  $z \sim 1.0$  (bottom). Each dot represents a mock observation of a single snapshot viewed from a single angle. In order to compare with the observational results from Kassin et al. (2007), 500 such images were chosen from the simulation set at random. Red points are mock observations where both galaxies are present in the slit (i.e. close encounters and the merger remnant), and black points are mock observations of single simulated galaxies. In the TF plots, the solid line is the high-redshift TF ridge line from Conselice et al. (2005), with the dotted lines representing the scatter. As in Kassin et al. (2007), a significant number of the simulated galaxies scatter to low  $V_{\text{rot}}$ . In the observations, these galaxies have disordered or compact morphologies. Similarly, in the simulations, the majority of the cases scattered to low  $V_{\text{rot}}$  are either undergoing or have recently undergone an encounter. In the  $S_{0.5}$  plots, the solid line is the fit to the observed  $S_{0.5}$  relation at  $z \sim 1.0$ , and the dotted lines depict scatter in the relation. The dashed line is the best fit to the simulations. Slopes ( $m$ ), zero points ( $y_0$ ), and scatters ( $\sigma$ ) for each fit are listed ( $y = y_0 + mx$ ). Including velocity dispersion greatly reduces the scatter and brings the progenitors, disturbed galaxies, merging galaxies, and merger remnants onto a single kinematic relation. The relation and scatter found for the simulated galaxies are comparable to the observed relation. Numbers on the plots show the location of the various numbered merger stages from Figure 1. The bottom panel has no ‘2’ because it overlaps ‘1’.

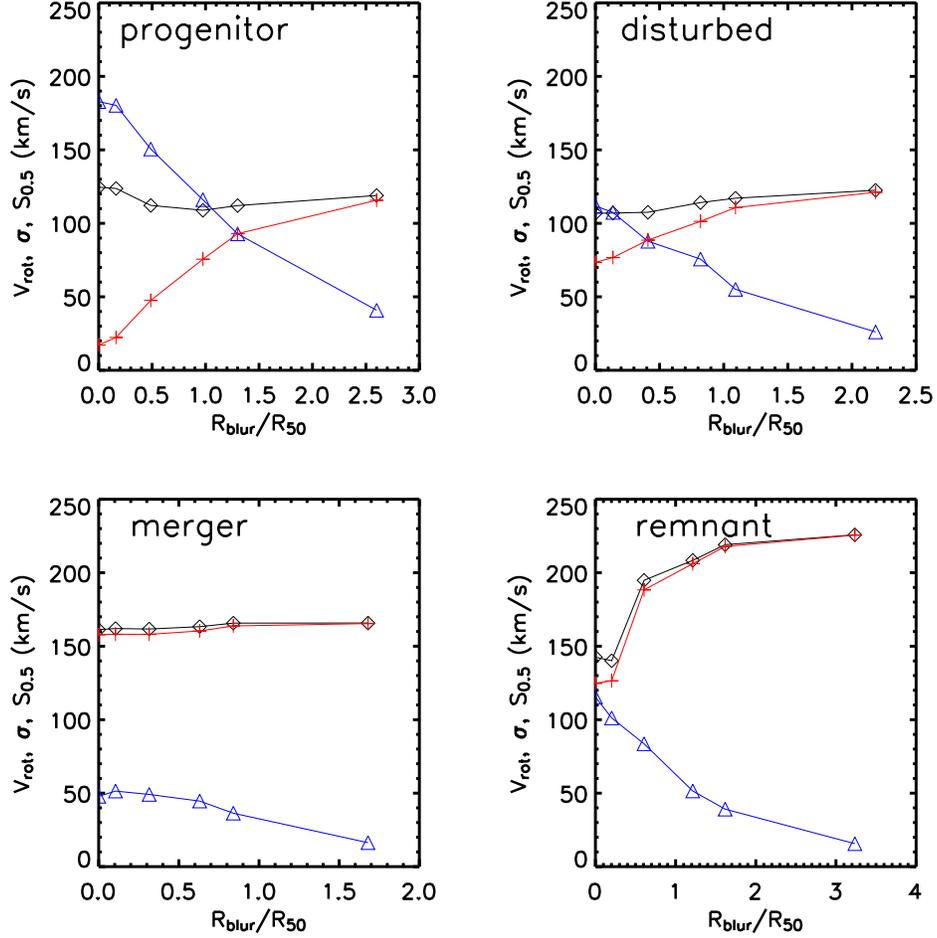


Fig. 3.— Effect of blurring on kinematics. We take the four snapshots from our fiducial Sbc merger (undisturbed disk=top left, disturbed disk=top right, merger=bottom left, and remnant=bottom right) mock observed at  $z = 1$ , and analyze the kinematics after blurring the particle positions by gaussians with  $\sigma$ 's of  $0.0''$ ,  $0.1''$ ,  $0.3''$ ,  $0.6''$ ,  $0.8''$ , and  $1.6''$ . Blurring is normalized using the (unblurred) radius that contains 50% of the stellar mass ( $R_{50}$ ). Lines and symbols are rotation velocity (blue triangles),  $\sigma$  (red crosses), and  $S_{0.5}$  (black diamonds). Since the physical radii are different for each stage, and the blurring is for specific angular scales, each plot shows a different range of  $R_{50}/R_{\text{blur}}$ .

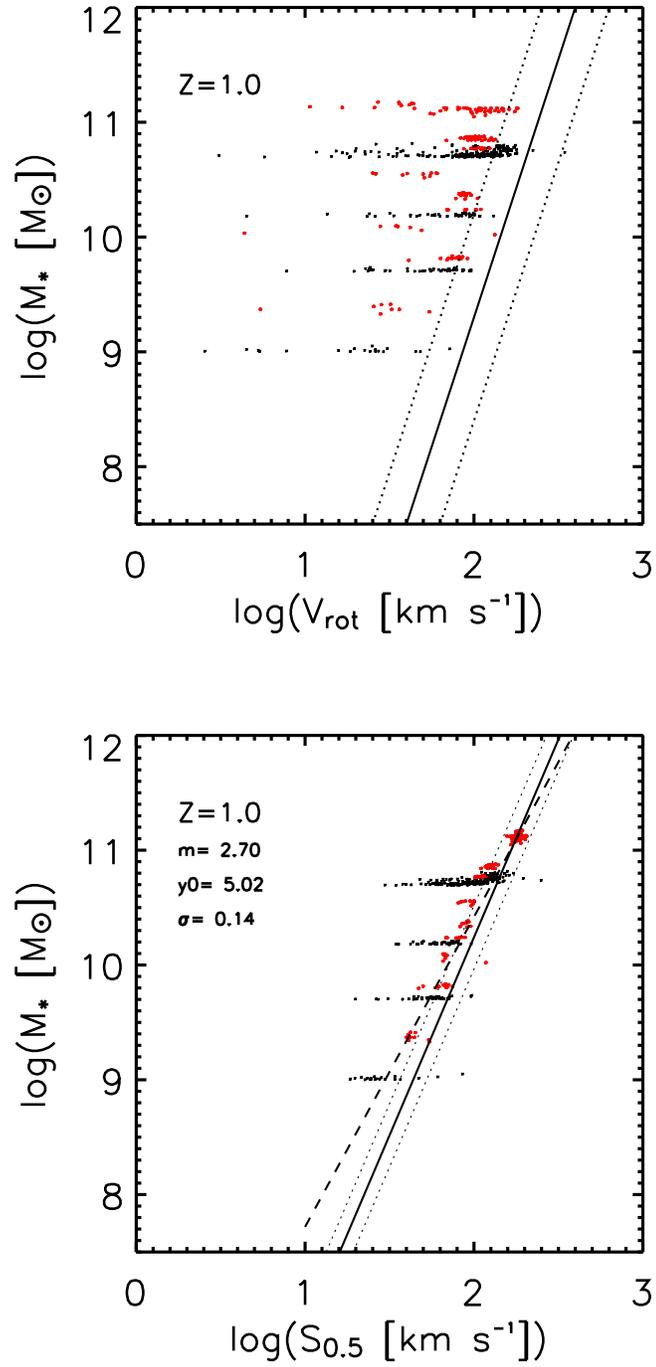


Fig. 4.— The Stellar Mass TF and  $S_{0.5}$ -Stellar Mass relations analogous to Figure 2 with the analysis from the simulations done using only new star particles.

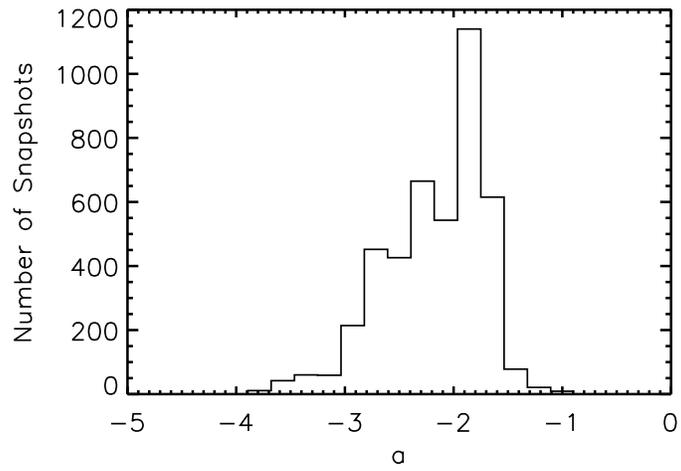


Fig. 5.— Histogram of the power law slope fit to the density profiles near  $R_{50}$  of each snapshot in the simulation set.

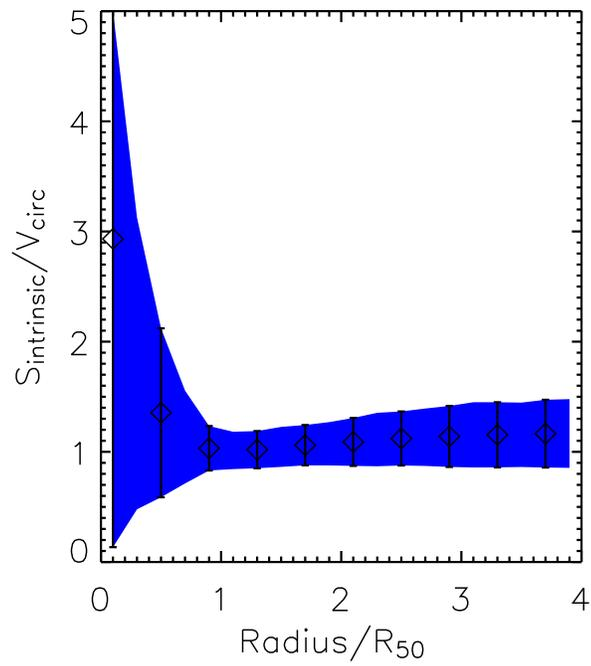


Fig. 6.— Ratio of  $S_{\text{intrinsic}}$  and  $V_{\text{circ}}$  as a function of radius averaged over all simulation snapshots and normalized to  $R_{50}$ . Blue range shows the  $1\sigma$  scatter in the profiles. At radii larger than  $\sim R_{50}$ ,  $S_{\text{intrinsic}}$  is a good estimator of total enclosed mass.

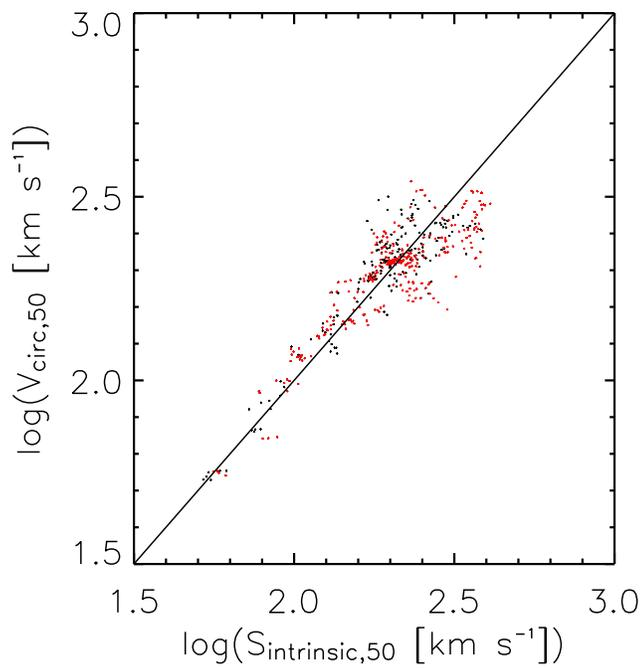


Fig. 7.— Relation between intrinsic  $S_{\text{intrinsic}}$  and  $V_{\text{circ}}$  at  $R_{50}$  as observed in the galaxy merger simulations. Red points are cases for which both galaxies were analyzed together, most of which are remnants. The  $x = y$  line shows the rough equivalence of  $S_{\text{intrinsic}}$  and  $V_{\text{circ}}$ .

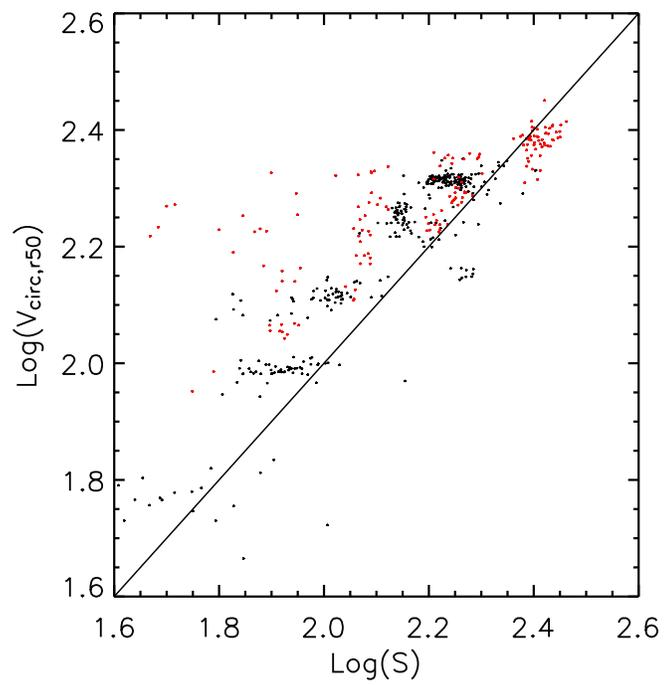


Fig. 8.— Relation between  $S_{\text{observed}}$  and  $V_{\text{circ}}$  as measured at  $R_{50}$ . Red points are cases for which both galaxies are analyzed together. The line plotted is the  $x=y$  line, demonstrating the correspondence between the two values.